

Electron Lambda-Tomography

Eric Todd Quinto ^{*}, Ulf Skoglund [†], and Ozan Öktem [‡]

^{*}Department of Mathematics, Tufts University, Medford, MA, U.S.A., [†]Department of Cell and Molecular Biology, Karolinska Institutet, Stockholm, Sweden, and [‡]CIAM: Center for Industrial and Applied Mathematics, KTH - Royal Institute of Technology, Stockholm, Sweden

Submitted to Proceedings of the National Academy of Sciences of the United States of America

Filtered Back-Projection and Weighted Back-Projection have long been the methods of choice within the electron microscopy community for reconstructing the structure of macromolecular assemblies from Electron Tomography data. In this paper we describe a novel reconstruction method, Electron Lambda-Tomography. This method enjoys the benefits of the above mentioned methods, namely speed and ease of implementation, and also addresses some of their shortcomings. In particular, compared to these standard methods, Electron Lambda-Tomography is less sensitive to artifacts that come from structures outside the region that is being reconstructed.

Electron tomography | Local tomography | Lambda Tomography | Limited Angle Tomography | Microlocal Analysis

Abbreviations: ART, Algebraic Reconstruction Technique; ET, Electron Tomography; ELT, Electron Lambda-Tomography; FBP, Filtered Back-Projection; PSF, Point Spread Function; ROI, Region of Interest; SIRT, Simultaneous Iterative Reconstruction Technique; TEM, Transmission Electron Microscope; TMV, Tobacco Mosaic Virus; WBP, Weighted Back-Projection

Introduction

This paper describes a new reconstruction method applicable to ET. The rigorous mathematical description of the method and its application to ET is given in [1]. Here we concentrate on the functionality of the method in an experimental setting with tests on real ET data. Furthermore, we derive a heuristic explanation for its advantages and also guidelines for its usage. Finally, we compare it with the most widely used method in the field, namely FBP/WBP. In this context, it should be mentioned that other reconstruction methods have also been developed and applied to ET. Iterative methods, such as ART and SIRT [2, 3], became practically applicable to ET only after regularization through early stopping. A clever discretization, based on Kaiser-Bessel window functions (blobs), was combined with strongly over-relaxed ART and then applied to ET data in [4, 5, 6]. Another approach is based on variational regularization where in [7, 8] relative entropy regularization is applied to ET. For more on these other approaches and their merits, we refer to [9, section 10.2], [10], and [11].

We begin with a very brief introduction to ET including a discussion of the various data collection geometries and a mathematical formulation of the structure determination problem in ET. This is followed by a brief outline of the FBP and WBP methods. We then move on to our algorithm, Electron Lambda-Tomography (ELT), that is based on two-dimensional Lambda Tomography [12, 13, 14]. However, ELT is also valid for a broad range of three-dimensional data acquisition geometries. It is a novel method that maintains the main benefits of the FBP and WBP methods, namely speed and ease of implementation, while addressing some of the shortcomings. In particular, ELT is generally less sensitive to artifacts that come from structures outside the ROI than these other methods. We conclude by providing examples of reconstructions obtained by ELT from real and simulated ET data.

Basic notation We now introduce notation used throughout the paper. We let \mathbb{R} denote the set of real numbers and \mathbb{R}^+ the set of positive real numbers. The three-dimensional space is denoted by \mathbb{R}^3 and the unit sphere in \mathbb{R}^3 , *i.e.* the set of all orientations in three-dimensional space, is denoted by S^2 . Furthermore, “:=” in equations will mean “defined as”.

Next, given a function f defined in three-dimensional space, the *projection* $\mathcal{P}(f)$ of f is defined as

$$\mathcal{P}(f)(\omega, \mathbf{x}) := \int_{-\infty}^{\infty} f(\mathbf{x} + t\omega) dt. \quad [1]$$

In the mathematics literature, $\mathcal{P}(f)$ is called the *X-ray transform* of f . Note that when f is represented by its voxel values in three-dimensional space, then $\mathcal{P}(f)(\omega, \mathbf{x})$ is essentially the sum of the values of f in the voxels that lie on the line through the point \mathbf{x} that has direction given by ω .

Finally, in some cases we choose to express formulae explicitly in a specific coordinate system (x, y, z) in \mathbb{R}^3 . In such case we will make use of the following convention: the x -axis is parallel the tilt-axis and the z -axis is parallel to the optical axis of the microscope at 0° tilt-angle.

Electron Tomography

Data collection geometry. Many tomographic experimental setups, including ET, yield data recorded on a detector that attains different orientations w.r.t. the specimen whose internal structure we seek to recover. In case of ET, each recorded TEM image is associated to a tilt-angle which in turn uniquely specifies an orientation of the specimen w.r.t. the optical axis of the TEM. Hence, the tilt-angle can equally well be re-interpreted as an orientation of the TEM detector w.r.t. the specimen. The data in a tilt-series constitutes a series of TEM images where the tilt-angle lies on a curve S of directions in three-dimensional space. Below, we explicitly describe this curve for each of the standard data acquisition geometries in ET.

Single-axis tilting: Here the specimen is rotated around a single axis perpendicular to the optical axis of the TEM. Then, the curve S is part of a longitude circle on the sphere, *i.e.* expressed in the (x, y, z) -coordinates

$$S := \left\{ (0, \sin(\theta), \cos(\theta)) : -\theta_{\max} \leq \theta \leq \theta_{\max} \right\}. \quad [2]$$

In the above, θ_{\max} corresponds to the largest tilt-angle which is approximately 60° .

Reserved for Publication Footnotes

Multi-axis tilting: In this case more than one single-axis tilt-series data series are taken. The curve S is given as the union of a number of single axis curves (see [2]) rotated around the z -axis. Dual axis tilting corresponds to the case where two single axis data sets are taken and fused in the above manner.

Slant tilting: For fixed $0 < \alpha < \pi/2$, the curve S is the set of angles α radians from the vertical z -axis. Hence, S is a latitude circle of the sphere. To get such data, one places the specimen in a plane of angle $\pi/2 - \alpha$ from the electron beam and rotates the specimen in that plane around a fixed point.

The model for image formation and the reconstruction problem. The idea that data from a TEM image can be interpreted as a “projection of the specimen” [15] underlies all current models for image formation used in ET. This is valid under certain approximations which are discussed in *e.g.*, [16, 9, 1]. Given these approximations, a processed tilt-series can be regarded as a finite sample of projections $P(f)(\omega, \mathbf{x})$ which are given by the tilt-angles ω contained in the curve S and \mathbf{x} in the detector plane. Here, the function $f: \mathbb{R}^3 \rightarrow \mathbb{R}^+$ is the “density” to be recovered and it is proportional to the electrostatic potential, which in turn describes the structure of the molecules in the specimen [17, 9]. Furthermore, we can represent the detector plane for tilt-angle ω by

$$\omega^\perp := \{x \in \mathbb{R}^3 : \mathbf{x} \cdot \omega = 0\}$$

which is the plane perpendicular to ω through the origin (the “physical” detector plane is a translate of this plane). If we introduce

$$\mathcal{M}_S := \{(\omega, \mathbf{x}) \in S^2 \times \mathbb{R}^3 : \omega \in S \text{ and } \mathbf{x} \in \omega^\perp\}, \quad [3]$$

then \mathcal{M}_S represents the collection of all lines with directions parallel to vectors in S (for each $\omega \in S$ and $\mathbf{x} \in \omega^\perp$, (ω, \mathbf{x}) represents the line parallel ω through \mathbf{x}). Therefore, a tilt-series will be a finite discrete sampling on \mathcal{M}_S and the reconstruction problem in ET can be stated as follows:

The reconstruction problem in ET: After suitable processing of the tilt-series, the reconstruction problem in ET can be reformulated as the problem of determining the real-valued function f , or some property thereof (*e.g.*, shape of the structures), from a finite sampling of $\mathcal{P}(f)$ on \mathcal{M}_S in [3] where the directions contained in the curve $S \subset S^2$ are given by the tilt-angles.

ET is often compared to medical tomography. However, the ET reconstruction problem has two important difficulties that do not arise in standard reconstruction problems in medical X-ray tomography. First, since traditionally only a small portion of the specimen is exposed to the electron beam, we are dealing with a *local* tomography problem, *i.e.* the tomographic data originates from a small ROI rather than from the entire specimen. This in turn means that, unless prior knowledge is being used as *e.g.* in [18], structures in the specimen can not be exactly recovered even if one were to have access to noise-free continuum data [19]. In [20] this issue is referred to as the unit cell being only partially defined. Second, due to the limited angular range of the tilt-angle, all of the standard data acquisition geometries described above yield *incomplete data* in sense that the curve S yields tilt-angles that do not circumscribe the specimen. This is known to introduce severe instability into the reconstruction problem.

To summarize, mathematically exact reconstruction for limited angle region of interest data is not possible even in

cases when one has noise-free continuum of data, and the reconstruction problem is severely unstable. However, as we shall see in Theorem 1, certain important features of the specimen can be reconstructed from such data.

Established analytic reconstruction schemes

In this section we discuss the FBP and WBP reconstruction schemes. Both are well established analytic reconstruction schemes frequently used within the ET community for solving the reconstruction problem in ET.

For tomographic data that satisfies a completeness condition¹; it can be shown that FBP yields a smooth approximate version of f , see *e.g.* [21, (2.34)] if the data is complete in a sense that can be made precise. Now, in ET all the data collection geometries mentioned before give rise to data that are not complete, hence for such data, FBP will not even recover a smooth approximate version of f .

The WBP approach is the Fourier space formulation of the FBP approach. For the same reasons, WBP will not recover an approximation of f from such ET data; the details are given in [10, section 6.1.1], see also [21, section 6.2.4].

Practical considerations. In the practical usage of FBP and WBP on real ET data, there are a number of additional issues that need to be considered. These are related to how the reconstruction operator is discretized and how to deal with noisy data.

First, in real applications of the FBP method, it is not desirable to attempt to recover the function exactly. The reason is simple; recovering f from finitely many samples of $\mathcal{P}(f)$ on \mathcal{M}_S is an inherently unstable problem even if the data were complete in the sense of footnote 1. Hence, a useful reconstruction method must include some kind of regularizing step even in the case of noise-free data, and in the FBP method this is achieved by choosing the filter such that the recovered function is a smooth approximation to f . As already mentioned, accurate and reliable recovery of f using the FBP scheme is possible only for complete data, which is not the case in the aforementioned data collection schemes for ET except in special cases in which there is some intrinsic symmetry of the object.

In the particular case of single-axis tilting each plane orthogonal to the tilt-axis can be dealt with separately. This allows one to reduce the three-dimensional reconstruction problem to a stack of two-dimensional reconstruction problems. Each of these are however limited angle region of interest problems in the plane due to the limited range of the tilt-angle. Still, in the current usages of the FBP method given single-axis tilting data, one simply chooses the filter in each slice as if one had complete data following the guideline in [22, 19]. In the electron microscopy community, this guideline is frequently referred to as Crowther’s criterion [17, p. 316]. The reconstruction is also often low-pass filtered in order to further regularize the solution.

¹The completeness condition is that the curve S fulfills *Orlov’s condition* which requires that the specimen is oriented in planes within the tilt-series that fill out the entire orientation space ($\cup_{\omega \in S} \omega^\perp = \mathbb{R}^3$), and data are given on all points in each detector plane [10, section 6.1.1]. Unfortunately, none of the standard ET data acquisition geometries described earlier satisfy Orlov’s condition. As an example, in the case of single-axis tilting with $\theta_{\max} = 60^\circ$, the planes ω^\perp for $\omega \in S$ do not meet the missing region, that is the wedges complementary to the wedge formed by the planes ω^\perp for $\omega \in S$. Both of the wedges in the missing region have an opening angle 60° . By definition, this data set is limited angle.

Electron Lambda-Tomography

As already mentioned, Electron Lambda-Tomography is an analytic reconstruction scheme. Therefore, it is based on the same assumptions as the FBP/WBP methods, namely that one can rephrase the reconstruction problem in ET as the problem of recovering a function f from projections $\mathcal{P}(f)$ sampled on \mathcal{M}_S .

In ELT we don't attempt to reconstruct f itself. Instead, we reconstruct a three-dimensional structure containing the information about f that can be stably retrieved, which turns out to be certain boundaries of the molecules. Furthermore, the recovered three-dimensional structure also shows what is inside and what is outside these boundaries, see Theorem 1 for a more precise statement.

The reconstruction operator. The ELT reconstruction operator that we consider is defined in [1] and is designed for projections sampled on \mathcal{M}_S . It reads as

$$\mathcal{L}_{S,\mu}(f) := \mathcal{P}_S^* ((-\mathcal{D}_S^2 + \mu) \mathcal{P})(f) \quad [4]$$

and we now explain the meaning of the above expression. \mathcal{P}_S^* denotes *backprojection operator* which is formally defined as

$$\mathcal{P}_S^*(g)(\mathbf{x}) := \int_S g(\boldsymbol{\omega}, \mathbf{x} - (\mathbf{x} \cdot \boldsymbol{\omega})\boldsymbol{\omega}) d\boldsymbol{\omega} \quad [5]$$

where g is a function in data space representing the projected data. Expressed in plain words, $\mathcal{P}_S^*(g)(\mathbf{x})$ is the sum of the data taken over all lines passing through \mathbf{x} (since $(\boldsymbol{\omega}, \mathbf{x} - (\mathbf{x} \cdot \boldsymbol{\omega})\boldsymbol{\omega})$ represents the line parallel $\boldsymbol{\omega}$ and passing through \mathbf{x}). The backprojection \mathcal{P}_S^* is a fundamental part of the FBP and WBP methods as well as ELT.

The derivative \mathcal{D}_S^2 is a second order differentiation in the detector plane along the tangential direction to the curve S , *i.e.*

$$\mathcal{D}_S^2 g(\boldsymbol{\omega}, \mathbf{y}) := \left. \frac{d^2}{ds^2} g(\boldsymbol{\omega}, \mathbf{y} + s\boldsymbol{\sigma}) \right|_{s=0} \quad [6]$$

where $\boldsymbol{\sigma}$ is the unit tangent to S at $\boldsymbol{\omega} \in S$ (in direction of increasing parameter).

Observe that ELT differs from FBP only in that the filter used in FBP is replaced by the sum $-\mathcal{D}_S^2 + \mu$. In contrast to the FBP method, $\mathcal{L}_{S,\mu}(f)$ is not an approximation of f ; $\mathcal{L}_{S,\mu}(f)$ replaces the filters in FBP/WBP by the simpler filter $(-\mathcal{D}_S^2 + \mu)$. The relation between $\mathcal{L}_{S,\mu}(f)$ and f is given by the microlocal regularity principle stated now. For the mathematically precise formulation and proof we refer to [1].

Theorem 1. *One can reconstruct a (molecular) boundary at a point \mathbf{x} whenever there is a projection in \mathcal{M}_S (the continuum data set) along a line (electron path) through \mathbf{x} that is tangent to this boundary. Moreover, such "visible" boundaries of f will be boundaries of $\mathcal{L}_{S,\mu}(f)$. Finally, the recovery of such visible boundaries is mildly ill-posed so it is possible to stably detect them in practice.*

This principle is illustrated in the reconstructions from simulated data (Fig. 2) and from real TMV data (Figs. 4 and 5). We now illustrate the principle for the simulated data. In the reconstructions from simulated data, the angular range of tilts is $\pm 60^\circ$ from the z -axis. Therefore, according to Theorem 1, the visible boundaries will be those tangent to lines in the data set. Therefore, they will be on the boundary circle between -60° and 60° and 120° to 240° . These are exactly the boundaries that are most clearly visible in both the ELT and the FBP reconstruction in Fig. 2. Neither algorithm images the boundaries in the invisible directions, and this is predicted by Theorem 1. One can see from Fig. 2b how the

ELT reconstruction highlights the visible boundaries of the disk compared with the FBP reconstruction in Fig. 2a.

Note that $\mathcal{L}_{S,\mu}$ is useful for ET because the algorithm reconstructs two important types of features of f . The pure Lambda reconstruction term (derivative term),

$$\mathcal{P}_S^* (-\mathcal{D}_S^2 \mathcal{P})(f), \quad [7]$$

emphasizes differences in data that occur at boundaries. In other words, the pure Lambda term picks up visible boundaries as given by Theorem 1. However, it does not distinguish interiors from exteriors since the derivative in these areas is typically small. The pure backprojection reconstruction term (μ term),

$$\mathcal{P}_S^* (\mu \mathcal{P})(f), \quad [8]$$

is an averaged version of f . To see this, assume the value of f is large (resp. small) near a point \mathbf{x} . Then the data on lines through \mathbf{x} will, in general, be large (resp. small) and the μ term $\mathcal{P}_S^* (\mu \mathcal{P})(f)$ will be large (resp. small). Thus the μ term adds contour to the reconstruction and allows one to distinguish objects from their surrounding. One can see this mathematically by noting that $\mu \mathcal{P}_S^* \mathcal{P}(f)(\mathbf{x})$ is a convolution of f with $c/|\mathbf{x}|$ on a cone representing the lines in the limited data set (see [1, 23] for specific calculations). The sum in [4] defining $\mathcal{L}_{S,\mu}(f)$ will therefore sharpen boundaries and highlight interiors of objects, as we will show using simulated and real data.

Practical considerations. So far, we have introduced two important parameters: μ and the width of the derivative kernel. In the actual implementation of $\mathcal{L}_{S,\mu}$ in the ET setting, the \mathcal{D}_S^2 operator in [4] is evaluated using a filter that is a smoothed version of the second derivative (a smoothed central second difference), and the half-width of the filter is determined by the noise characteristics of the data, the sensitivity of the detectors and the contrast of the specimen as given in the discussion on Reconstruction Protocol below.

The other important parameter is μ . In [14], a paradigm to choose μ is given where a feature is selected and μ is chosen so that the $\mathcal{L}_{S,\mu}$ reconstruction is closest to flat inside a specific feature. This is possible, in general, because the pure Lambda reconstruction term, [7] curves down inside regions and the pure backprojection term [8], term curves up. The first author's student T. Bakhos has tested this, and it works well with low noise data and as long as there is only one main region of interest in the reconstruction region. However, in ET, noise and sparsity of data suggest that more *ad hoc* methods are better.

Because the ET data are so noisy, we convolve on the detector plane in the direction perpendicular to $\boldsymbol{\sigma}$ (see [6]), and this brings up a third parameter, the kernel width of this convolution, which for single-axis tilting is just averaging over slices. As with the derivative kernel, this width is correlated with the noise characteristics of the data. This corresponds to the normal way to regularize FBP or WBP reconstruction. A starting point for setting the width of these kernels could be calculated according to Crowther's Criterion on each slice. This step can be done either slice by slice or after the fact, in 3D, for the whole reconstruction. The reconstruction method is fast enough to allow extensive experiments to calculate optimal parameters.

Advantages of Electron Lambda-Tomography

The FBP/WBP methods have been extensively used over the years and they are well known to deliver a decent result when reasonable parameters are given. The improvement of ELT

over FBP/WBP is nevertheless quite clear and based on the intrinsic differences of the methods. Mathematically, FBP and WBP require complete data (see Footnote 1) to accurately reconstruct, but ET data is not complete. ELT being local, does not require complete data.

One can see the advantages of locality in several ways. If one compares the convolution kernels for ELT and FBP as done in [1, Figure 1]. The ELT kernel is local— it is zero away from the origin, but the FBP kernel is not. In fact, the FBP kernel in that figure has oscillations on the interval where the ELT kernel is zero that are about 7% of the maximum amplitude. This illustrates the fact that ELT needs only data through the ROI to reconstruct the structures but FBP needs all data on the detector plane (which is not given in ET). Comparing PSF's in Fig. 1, one sees the ELT reconstruction operator has a much more localized PSF than FBP. The “X” or wings at the end of the angular range on both the FBP PSF and the ELT PSF are expected in any limited angle backprojection algorithm. In addition, because the PSF is less localized in the FBP case, the signal spread out and away from the real signal into the surrounding, causing a dilution of the actual signal relative to the back ground. This renders the FBP more noisy than the ELT in general, and thus there is a higher chance to lose a weak signal altogether in the FBP case.

In Fig. 2 we see the effects of shadowing from far away as well as nearby densities. In general they cause troughs that are clearly less for ELT than FBP reconstructions. To only have small troughs is important because deep troughs might mask smaller nearby objects. Furthermore, the lambda boundaries are better defined. Taken together this leads to less disturbances in the structures themselves in the ELT density.

Examples

In this section we compare reconstructions obtained by FBP and ELT. We start out with simulated two-dimensional data to illustrate the properties of the ELT operator. Next, we move on to real ET data.

Simulated two-dimensional data. This experiment illustrates the fundamental properties of ELT. First, we compare ELT and FBP reconstructions of a single disk (Figs. 2a and 2b). Then, we compare ELT and FBP reconstructions for the same disk plus two objects outside the ROI (Figs. 2c and 2d). This will show the effects of locality of the ELT operator. The ROI is a disk of radius two units and the phantom in Figs. 2a and 2b consists of one disk of radius 0.5 units centered at the origin (see Fig. 2 for the data geometry). Parameters are chosen to be essentially the same as the ones we used in our experiments with real data.

The FBP reconstruction in Fig. 2a shows very dark triangular troughs to the left and to the right of the disk that could mask details near the disk. Although the triangles are visible in the ELT reconstruction in Fig. 2b, they are less pronounced.

The reconstructions in Figs. 2c and 2d include two disks outside the ROI of radius 0.5 centered at (2.6, 0) and (−2.6, 0) and density 25 times that of the origin centered disk. Note that these disks affect both the ELT and FBP reconstructions since they affect data through the ROI. At the left and right boundaries of both reconstructions are triangular troughs from these added disks, but the triangles are much darker in the FBP reconstruction than the ELT reconstruction. The boundary of the central disk is highlighted in our

ELT reconstructions compared to the FBP one, and this helps visualize the central disk.

To summarize, the boundaries are highlighted in the ELT reconstruction compared to FBP and ELT can be less sensitive to structures outside of the ROI.

Real ET data. We tested the behavior of ELT versus FBP on a real *in-vitro* biological sample of TMV supplied by Dr. J. Butler, MRC laboratory for molecular biology, Cambridge, UK. The rationale for choosing this sample was that the structure of the TMV is well-known. The FBP algorithm used on this data is the optimized version used at the Department of Cell and Molecular Biology at the Karolinska Institute in Stockholm.

The TMV is made up of a helical cylinder with an outer diameter of about 18 nm and an inner cylindrical hole along the helical axis with a diameter of about 4 nm [24, 25]. The size and regularity of the TMV deems it a suitable sample for a simple comparison— even at the rather low resolution inherent in this particular experiment at about 7.5 nm resolution. The contrast between the protein (and RNA) mass is enough to enable the visualization of the hole despite it being smaller than the resolution of 7.5 nm. A part of this enabling situation is the fact that the hole is a cylinder and continues along the entire virus.

Specimen preparation: The concentration of TMV particles was 3 mg/mL and the colloidal gold markers added for alignment had a diameter of about 10 nm. The gold markers were coated with BSA (Amersham AuroProbe™ EM protein A G10) and washed to remove unbound BSA. The specimen was placed on carbon-coated Quantifoil™ R2/2 grids that were glow discharged on both sides. A Vitrobot™ was used for the vitrification process at 100% humidity with a 2 s blotting time. After vitrification, we obtained a specimen consisting of TMV particles embedded in a slab of vitrified aqueous buffer with a thickness slightly less than 115 nm.

TEM imaging protocol: The imaging was done at Sidec AB with a FEI Tecnai™ Polara with a FEG at 300 kV. The detector was a Gatan UltraScan™ 1000 with a CCD of 14 μm pixel size giving 2048 × 2048 pixels per image and a sensitivity of about 5 counts per electron. The magnification was calibrated to 19830× giving a pixel size after magnification of 0.5757 nm. The *low-dose tilt-series* was collected at 10 μm underfocus following the single axis tilting scheme with 65 low-dose images collected at every second degree. The total dose used for the low-dose tilt-series was 1230 e[−]/nm², which gives an average dose of 18.92 e[−]/nm² (or 6.27 e[−]/pixel) in one image in the low-dose tilt series. After the low-dose tilt series had been recorded, a *post-image* was collected at considerable higher dose at 0° tilt-angle, but still at 10 μm underfocus, enabling a better view of the imaged area of the specimen.

TEM images of the TMV sample are shown in Fig. 3. The 200 × 200 pixel square region insert in Fig. 3 is overcasting an area slightly to the left in the post-image. This square region shows the projection of the ROI that is reconstructed. It contains two vertical and five horizontal TMV particles crossing the ROI and that we expect to see in the ensuing 3D reconstructions. The reason for choosing the ROI in such an area is to see how the ELT and FBP reconstructions are compromised in a crowded region. In addition we have an enlarged version of the ROI insert at the top right and lower right. The lower right shows the same area from the low-dose not-tilted specimen with 200 e[−]/nm². The whole Fig. 3 image spans 2048 × 2048

pixels with 0.5757 nm pixel size, thus covering 1179 nm in each direction.

Data pre-processing: The images in the low-dose tilt-series were aligned using the colloidal gold markers. The average alignment error over all the tilts was less than 0.75 nm (*i.e.* about 1.3 pixels). From the aligned images we then extracted a data set which in turn served as input data for the 3D reconstructions of the ROI. The ROI has a size of $200 \times 200 \times 200$ voxels and it was calculated from an image support of 300×300 pixels from the aligned images in the low-dose tilt-series.

Reconstruction protocol: Crowther's criterion applied to this data dictates using a reconstruction kernel with a half-width of 4 nm in FBP. In order to compensate for the loss in resolution due to missing data, following [26], the kernel half-width is increased by about 50%. Furthermore, the low signal-to-noise-ratio in data motivates further increase in the kernel half-width to 7.5 nm.

For ELT, the half-widths of the convolution kernel representing \mathcal{D}_z^2 in [4] (the derivative kernel) and the convolution representing the averaging over slices (slice averaging kernel) are related to the signal-to-noise-ratio in the data. This in turn is related to the sensitivity of the detector, the contrast in the specimen, and the dose. In general one can use larger half-widths to smooth the reconstruction more when the signal-to-noise ratio in the data decreases. To prescribe a specific protocol for choosing the half-width would require extensive testing on a large number of specimens. However, it turns out that the half-widths can be chosen close to the above value of 7.5 nm used for the FBP. We can however account for the anisotropy in resolution caused by limited data and we settle for a half-width of 6 nm for the derivative kernel and 7 nm for the slice averaging kernel.

The TEM data as well as the 3D reconstructions of TMV are represented in Figs. 3, 4, and 5. Note that it is not easy to see the centrally placed hole even in the high-dose post-image shown in Fig. 3. This is due partly to induced beam damages and partly due to the large defocus-induced extra contrast shadowing the fainter low density hole. The hole is however

visible in the 3D reconstructions. The Fig. 5 is a volumetric displays of the FBP and ELT reconstructions. Furthermore, the alignment of the tilt-series showed that the densities in Figs. 5 should be rotated about 11° clockwise to exactly superimpose on the ROI insert of the ROI shown in Fig. 3.

In the visualization in Figs. 4, and 5, the emphasis is put on the two TMV particles that can be seen passing vertically through the ROI insert in Fig. 3. The two virions pass on top of the five others, and in Fig. 4 we show a 1.15 nm thick slice through the tomograms showing the central part of the virions. The cylindrical hole is clear in both FBP and the ELT tomograms (Figs. 4a and 4b, respectively). The diameter of the TMV particle can be estimated to be just below 18 nm for both virions (the side of the square image is 200 pixel, or 115 nm), and the hole between 4.5 and 5 nm. These values agree with the published structural parameters for TMV [24, 25] and are used as benchmarks to justify our choices of half-widths described in the reconstruction protocol above. Furthermore, it is clear in Fig. 4 that the FBP density is more cluttered than the ELT one, and that *e.g.* the virion is more connected in the ELT density. In Fig. 5 we show a $200 \times 200 \times 160$ voxel sub-region of the ROI reconstructed by FBP and ELT. The sub-region is viewed along the beam direction having the tilt-axis horizontal. The thresholds used for contouring the two tomograms have each been selected so that the structural parameters (outer diameter and diameter of the inner cylindrical hole) related to the virions in the tomograms agree with the published ones. Still, it's clear that the ELT tomogram is much easier to interpret due to the obviously lower clutter-level. The virions are also more disconnected in the FBP tomogram when this threshold is used for contouring. If we decrease the threshold level, the background clutter makes the analysis difficult. One can also see the increased clutter in FBP versus ELT when one rotates the 3D reconstructions.

ACKNOWLEDGMENTS. We are grateful to Sara Sandin and Lars-Göran Öfverstedt for acquiring the TMV tilt-series data we used. The first author was supported by NSF grant 0456858. He thanks the Wenner Gren Stiftelserna for grants over the years that have greatly aided this research. He thanks Tufts University Faculty Research Awards Committee and Sidec, Stockholm, for their generous support.

1. E. T. Quinto and O. Öktem. Local tomography in electron microscopy. *SIAM Journal of Applied Mathematics*, 68(5):1282–1303, 2008.
2. R. Schoenmakers, R. A. Perquin, T. F. Fliervoet, and W. Voorhout. High resolution, high throughput electron tomography reconstruction. *Microscopy and Microanalysis*, 11 (suppl 2):312–313, 2005.
3. W. Voorhout, F. De Haas, P. Frederik, R. Schoenmakers, W. Busing, and D. Hubert. An optimized solution for cryo-electron tomography. *Microscopy and Microanalysis*, 12:1110–1111, 2006. Extended abstract of a paper presented at Microscopy and Microanalysis 2006 in Chicago, Illinois, USA, July 30 – August 3, 2006.
4. R. Marabini, G. T. Herman, and J.-M. Carazo. 3D reconstruction in electron microscopy using ART with smooth spherically symmetric volume elements (blobs). *Ultramicroscopy*, 72:53–65, 1998.
5. R. Marabini. Three-dimensional reconstruction from reduced sets of very noisy images acquired following a single-axis tilt schema. Application of a new three-dimensional reconstruction algorithm and objective comparison with weighted backprojection. *Journal of Structural Biology*, 120:363–371, 1997.
6. J.-M. Carazo, G. T. Herman, C. O. S. Sorzano, and R. Marabini. Algorithms for three-dimensional reconstruction from the imperfect projection data provided by electron microscopy. In J. Frank, editor, *Electron Tomography. Methods for Three-Dimensional Visualization of Structures in the Cell*, chapter 7, pages 217–243. Springer Verlag, 2nd edition, 2006.
7. U. Skoglund, L.-G. Öfverstedt, R. M. Burnett, and G. Bricogne. Maximum-entropy three-dimensional reconstruction with deconvolution of the contrast transfer function: a test application with Adenovirus. *Journal of Structural Biology*, 117:173–188, 1996.
8. H. Rullgård, O. Öktem, and U. Skoglund. A component-wise iterated relative entropy regularization method with updated prior and regularization parameter. *Inverse Problems*, 23:2121–2139, 2007.
9. D. Fanelli and O. Öktem. Electron tomography: A short overview with an emphasis on the absorption potential model for the forward problem. *Inverse Problems*, 24(1):013001, 2008.
10. O. Öktem. Reconstruction methods in electron tomography. In *Mathematical Methods in Biomedical Imaging and Intensity-Modulated Radiation Therapy (IMRT)*, pages 289–320, Pisa, Italy, 2008. Centro De Giorgi. CRM Series, Volume 7.
11. L. Norlén, U. Skoglund and O. Öktem. Molecular cryo-electron tomography of vitreous tissue sections: Current challenges. *Journal of Microscopy*. Accepted for publication, 2009.
12. E. I. Vainberg, I. A. Kazak and V. P. Kurozaev, Reconstruction of the internal three-dimensional structure of objects based on real-time integral projections. *em Soviet Journal of Nondestructive Testing*, 17:415–423, 1981.
13. A. Faridani, E. L. Ritman, and K. T. Smith. Local tomography. *SIAM Journal of Applied Mathematics*, 52:459–484, 1992.
14. A. Faridani, D. Finch, E. L. Ritman, and K. T. Smith. Local tomography II. *SIAM Journal of Applied Mathematics*, 57:1095–1127, 1997.
15. H. P. Erickson and A. Klug. Measurement and compensation of defocussing and aberrations by Fourier processing of electron micrographs. *The Philosophical Transactions of the Royal Society, Series B*261:105–118, 1971.
16. P. W. Hawkes. The electron microscope as a structure projector. In J. Frank, Ed., *Electron Tomography. Methods for Three-Dimensional Visualization of Structures in the Cell*, chapter 3, pages 83–111. Springer Verlag, 2nd edition, 2006.
17. P. A. Penczek and J. Frank. Resolution in electron tomography. In J. Frank, editor, *Electron Tomography. Methods for Three-Dimensional Visualization of Structures in the Cell*, chapter 10, pages 307–330. Springer Verlag, 2nd edition, 2006.
18. H. Yu and G. Wang. Compressed sensing interior tomography. *Physics in Medicine and Biology*. 54:2791–2805, 2009.
19. F. Natterer. *The Mathematics of Computerized Tomography*, volume 32 of *Classics in Applied Mathematics*. SIAM, 2001.
20. W. Hoppe and R. Hegerl. Three-dimensional structure determination by electron microscopy (nonperiodic specimens). In *Computer Processing of Electron Microscopic Images* (P. W. Hawkes, Ed.), pages 127:185 (Springer-Verlag, Berlin) 1980.

21. F. Natterer and F. Wübbeling. *Mathematical Methods in Image Reconstruction*, volume 5 of SIAM monographs on mathematical modeling and computation. SIAM, 2001.
22. A. Faridani. *Introduction to the mathematics of computed tomography*. In G. Uhlmann, editor, *Inside Out: Inverse Problems and Applications*, volume 47 of MSRI Publications, pages 1–46. Cambridge University Press, Cambridge, 2003.
23. E. T. Quinto, T. Bakhos, and S. Chung. *A local algorithm for Slant Hole SPECT*. In *Mathematical Methods in Biomedical Imaging and Intensity-Modulated Radiation Therapy (IMRT)*, pages 321–348, Pisa, Italy, 2008. Centro De Giorgi. CRM Series, Volume 7.
24. K. C. Holmes. *The structure and assembly of simple viruses*. In *Structural Molecular Biology. Methods and Applications* (D. B. Davies, W. Saenger and S. S. Danyluk, Eds.), pages 475–505 (Plenum-Press, New York) 1982.
25. P. J. G Butler, *Review Article: The Current Picture of the Structure and Assembly of Tobacco Mosaic Virus*. *Journal of General Virology*, 65:253–279, 1984.
26. M. Radermacher, *Three-dimensional reconstruction of single particles from random and nonrandom tilt series*, *Journal of Electron Microscopy Technique* 9:359–394, 1988.

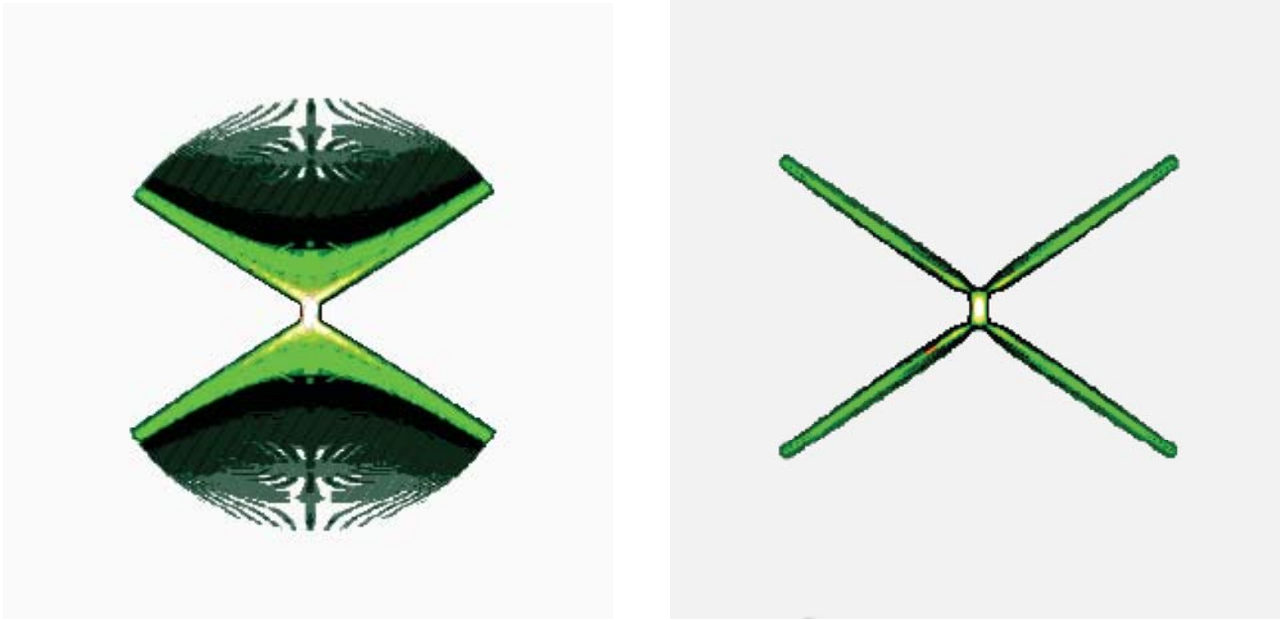
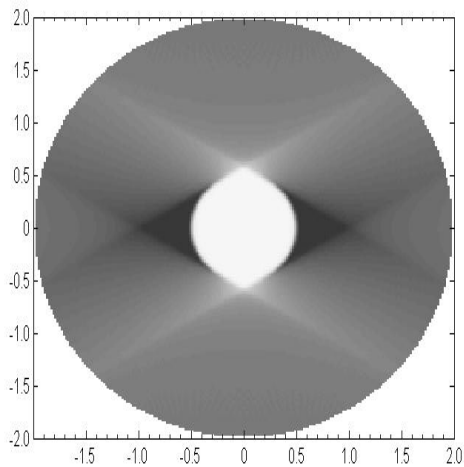
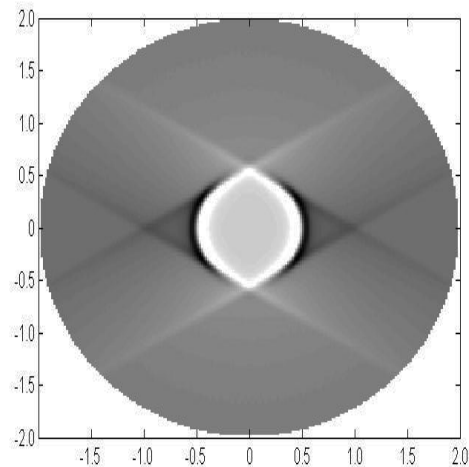


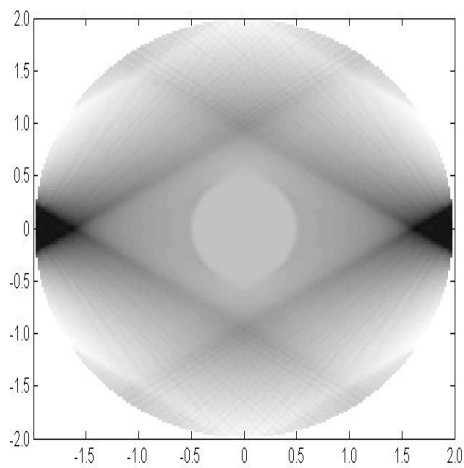
Fig. 1: A three-dimensional surface plot of the PSFs in FBP and in ELT for single axis tilting. The beam direction is vertical, and the tilt-axis is perpendicular to the plane. The maximum tilt-angle is 60° from the beam direction. The left image shows the PSF in FBP whereas the right image shows the PSF for standard ELT with a comparable width (and $\mu = 0$). We see that the ELT PSF in the right image is more localized than the standard FBP PSF in the left image.



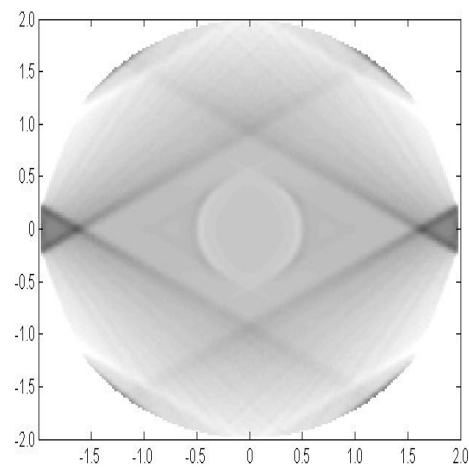
(a) FBP 2D reconstruction with no objects outside the ROI



(b) ELT 2D reconstruction with no objects outside the ROI



(c) FBP 2D reconstruction with two disks outside the ROI



(d) ELT 2D reconstruction with two disks outside the ROI

Fig. 2: FBP and ELT reconstructions of simulated data for one disk of radius 0.5 in a ROI that is a disk of radius 2. In the top two pictures, Figs. 2a and 2b, there is nothing outside the ROI. In the bottom two pictures, Figs. 2c and 2d, there are two disks of radius 0.5 centered at $(0, \pm 2.6)$ outside the region. The maximum tilt-angle is 60° from the z -axis (vertical) and 120 tilts are used with 200 projections per tilt. Note that the ELT reconstruction highlights boundaries and is less affected by objects outside the region than the FBP.

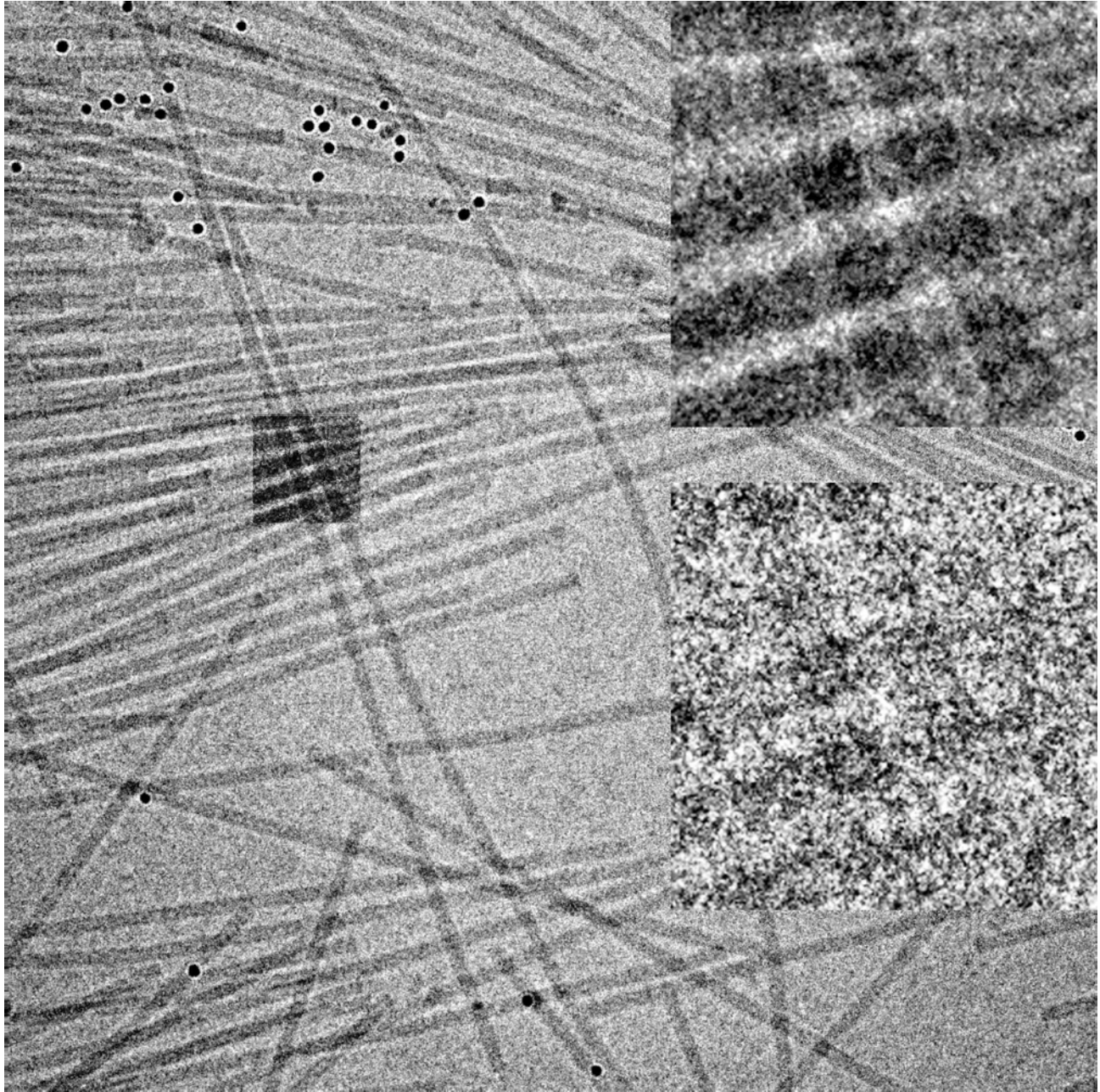
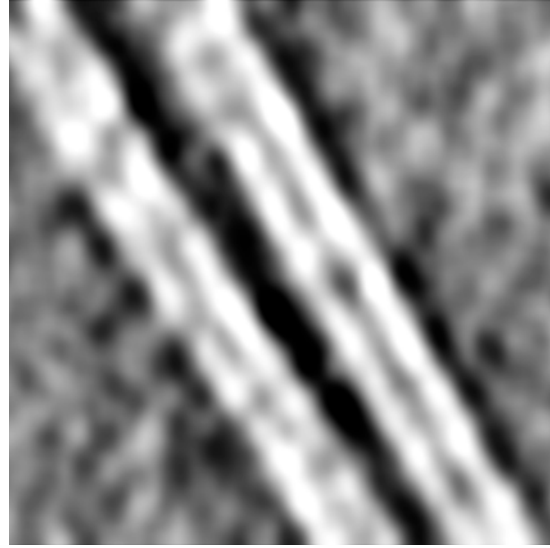


Fig. 3: TEM images of an *in-vitro* TMV specimen. The large region is the entire 2048×2048 pixel high-dose TEM image taken at the 0° tilt-angle with a $10 \mu\text{m}$ underfocus and recorded after the tilt-series has been collected (post-image). The small 200×200 pixel highlighted square slightly to the left shows the projection of the ROI onto the post-image. The reconstructions of the ROI are shown in Figs. 4 and 5. The upper right-hand square is a $4\times$ enlargement of the previously mentioned small square. Finally, the lower right-hand square is the projection of the ROI onto the low-dose image from the tilt-series corresponding to the 0° tilt-angle. This is one of the 65 TEM images that constitute the single axis tilt-series. The 10 nm golds are visible as black spots surrounded by a whitish “halo” caused by the large underfocus.

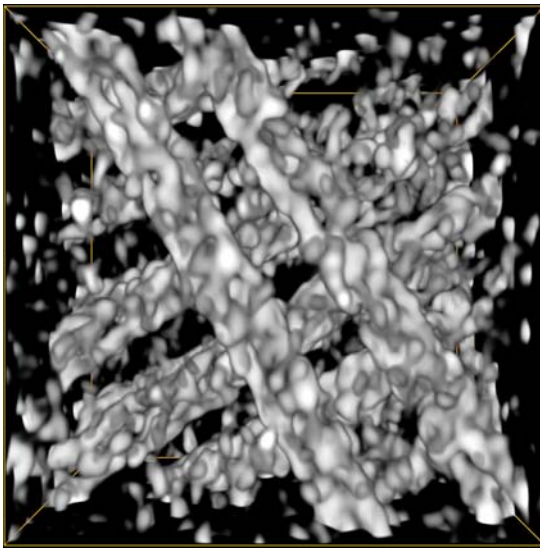


(a) Slice through the FBP tomogram.

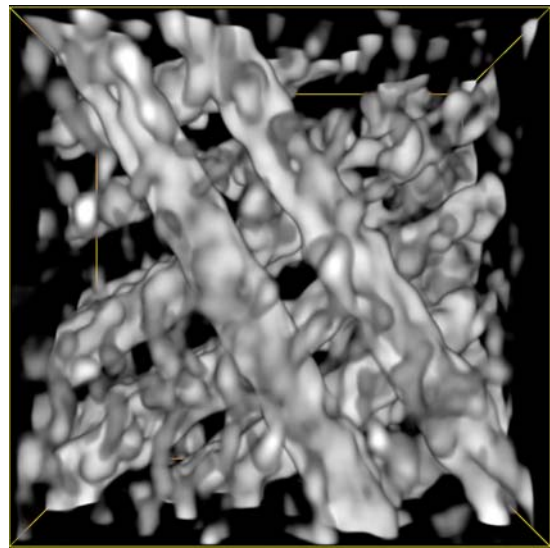


(b) Slice through the ELT tomogram.

Fig. 4: Volumetric displays of the FBP and ELT reconstructions of TMV. Emphasis is put on the two TMV particles that can be seen passing vertically through the ROI insert in Fig. 3. Shown is a 1.15 nm thick slice through the tomograms outlining the central part of the virions. The cylindrical hole is clear in both FBP and the ELT tomograms (Figs. 4a and 4b, respectively). The diameter of the TMV particle can be estimated to be just below 18 nm for both virions (the side of the square image is 200 pixel, or 115 nm), and the hole between 4.5 and 5 nm. These values agree with the published structural parameters for TMV [24, 25]. The FBP density is more cluttered and less connected than the ELT one. The maximum tilt-angle is 60° .



(a) FBP 3D tomography.



(b) ELT 3D tomogram.

Fig. 5: Volumetric displays of the FBP and ELT reconstructions of TMV. Shown is a $200 \times 200 \times 160$ voxel sub-region of the FBP and ELT reconstruction of the ROI. The sub-region is viewed along the beam direction having the tilt-axis horizontal. The thresholds used for contouring the two tomograms have each been selected so that the outer diameter of the virions agree with the known value. It's clear that the ELT tomogram is much easier to interpret due to the obviously lower clutter-level and that the virions are more disconnected in the FBP tomogram.